The Barcelona Ionospheric Mapping Function (BIMF) and its application to northern mid-latitudes

Haixia Lyu[1,2], Manuel Hernández-Pajares[1,3], Metin Nohutcu[4], Alberto García-Rigo[1], Hongping Zhang[2], Jingnan Liu[2]

[1] UPC-IonSAT, Universitat Politècnica de Catalunya, Barcelona, Spain

[2]GNSS Research Center, Wuhan University, Wuhan, China

[3]IEEC-CTE-CRAE, Institut d'Estudis Espacials de Catalunya, Barcelona, Spain

[4]Department of Geomatics Engineering, Hacettepe University, Ankara, Turkey

H. Lyu, e-mail: haixialv1987@gmail.com;

M. Hernández-Pajares, e-mail: manuel.hernandez@upc.edu;

M. Nohutcu, email: mnohutcu@hacettepe.edu.tr;

A. García-Rigo, e-mail: alberto.garcia.rigo@upc.edu;

H. Zhang, e-mail: hpzhang@whu.edu.cn;

J. Liu, e-mail: jnliu@whu.edu.cn.

Abstract A simple way of improving the GNSS user slant ionospheric correction from Vertical Total Electron Content (VTEC) models is presented in this paper. Indeed, the variable distribution of the free electrons of the ionosphere has a significant impact on Global Navigation Satellite Systems (GNSS). To correct it, a mapping function is required to convert from VTEC, provided in Global Ionospheric Maps (GIMs), to Slant TEC (STEC). Typical approaches assume a single ionospheric shell with constant height, which is unrealistic, especially for low-elevation signals. In order to reduce this error, we propose the Barcelona Ionospheric Mapping Function (BIMF), and its first implementation at northern mid-latitudes (BIMF-nml). BIMF is based on a climatic prediction of the distribution of the topside electron content fraction, regarding to the VTEC (hereinafter μ_2). But in practice no external data are required, which is convenient for applications. To evaluate its performance, we compare with STEC difference values directly measured from mid-latitude dual-frequency GPS receivers that have not been used in the computation of the VTEC GIMs under

assessment. It is shown that, compared to standard mapping functions used by the International GNSS Service (IGS) and Satellite Based Augmentation System (SBAS), the BIMF improves the STEC estimation. This happens not only for the UPC GIMs, which already use a tomographic model, with up to 15% of improvement during the whole 2014, but especially for the GIMs of other analysis centers, like the CODE GIMs and JPL GIMs with up to 32% and up to 29% of improvement respectively.

Keywords ionospheric mapping function, vertical total electron content, global ionospheric maps, shape function

Introduction

It is well known that ionospheric delay is one of the important factors influencing GNSS positioning accuracy, particularly for SPP (Standard Point Positioning). Using broadcast ionosphere model parameters, e.g., the Klobuchar model of GPS (Global Positioning System) (Klobuchar, 1987) or the NeQuick model for Galileo (European Commission, 2016), is an option for single frequency GNSS receivers with restricted accuracies. There are also several different approaches for single frequency users to mitigate the ionospheric error, such as empirical models, GIMs, and the numerical models provided by the SBASs (Satellite Based Augmentation Systems) to achieve better ionospheric corrections. GNSS users, who use these alternative approaches, need to convert vertical total electron content (VTEC) computed from ionospheric models to slant total electron content (STEC) for ionospheric delay correction. The relationship between them is described by ionospheric mapping functions. Traditionally, mapping functions are based on the single layer assumption, which assumes all the electron content is concentrated in a shell of infinitesimal thickness at a fixed height from 350 km to 450 km. Figure 1 represents the single layer approach where the ionospheric pierce point (IPP) is the intersection point of the signal path with the single layer, R is the mean radius of the earth, H is the height of the single layer from the ground level, and z and are zenith angles of the satellite at the receiver and IPP, respectively.

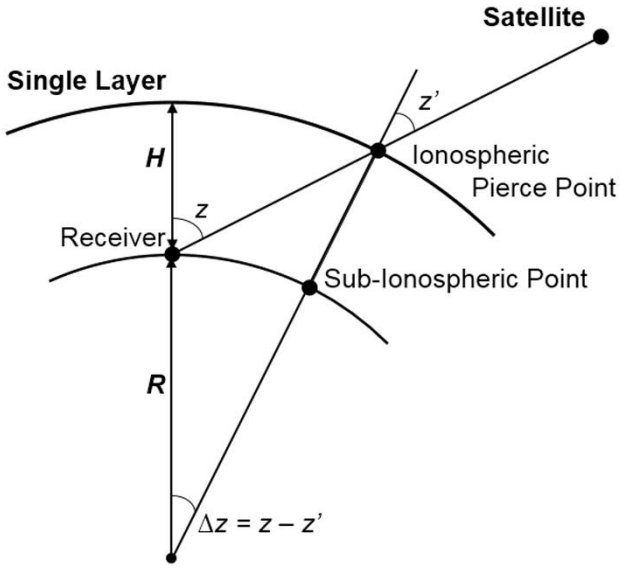

Fig. 1 Single layer model for the ionosphere (Schaer, 1999).

In fact, the ionospheric effective height, i.e. the optimal height to represent the ionospheric electron content within a single spherical and geocentric layer, mainly varies with geographical location, local time, season and solar activity as it depends on the electron density distribution and on the elevation angle above the horizon of the receiver-transmitter line-of-sight due to the nonlinear dependence of the mapping function on the ionospheric effective height. Komjathy (1996) analyzed the effects of using different ionospheric shell heights on VTEC estimates and satellite-receiver differential delays and also mentioned the concept of the varying ionospheric shell height. Niranjan et al. (2007) studied the variability of the electron density distribution in the Indian equatorial and low-latitude region and indicated that the IPP height could vary between 750 and 1500 km depending on the time and the season. Birch et al. (2002) concluded that the 350–400 km region is too low for an effective height, and a range of 750–1200 km is the better choice. Among other literature for Satellite-Based Augmentation Systems (SBAS), Komjathy et al. (2003) studied the range error introduced by using the WAAS thin-shell mapping function during the storm event in the mid-latitude regions. Lejeune et al. (2003) concluded that the equatorial slant-to-vertical conversion errors among other error sources result in large error bounds after analyzing the performance of SBAS ionospheric estimation algorithms in equatorial regions. Sakai et al. (2009) considered the vertical structure of the ionosphere by two models, which are the "Variable Height Shell" model, for which is difficult to measure the proper shell height, and

the "Multi-layer Shell" model, which causes larger residual error in some periods. Hoque and Jakowski (2013) adopted the Chapman layer assumption for describing the vertical electron density distribution of the ionosphere and Zus et al. (2016) used IRI model. Nevertheless, VTEC modeling from GNSS measurements is not our interest in this work. Our goal is user-oriented and to get more accurate STEC values from GIMs or other VTEC models. Moreover, in precise GNSS relative positioning, mostly based on dual-frequency carrier phase measurements such as Real-Time Kinematic (RTK) or Wide-Area RTK (WARTK, Hernández-Pajares et al. 2000a), the ionospheric delay information is important to users. When the distances among the reference stations increase, the ambiguity resolution success rate decreases due to the poor spatial dependence of atmospheric delay. If more accurate STEC information could be provided, the ambiguity resolution success rate improves (Hernández-Pajares et al. 2002).

In this context, we propose a new mapping function, called the Barcelona Ionospheric Mapping Function, and focusing in this work on northern mid-latitudes (BIMF-nml). Previously the topside electron content fraction regarding to VTEC, μ_2, was estimated during more than one Solar Cycle in the ionospheric tomographic runs performed by UPC to generate the corresponding Global Ionospheric Maps, GIMs, for IGS. On the basis of a climatic prediction of the distribution of μ_2, BIMF is more realistic as compared to the traditional approach. Concretely, BIMF-nml provides μ_2 in terms of a low-degree polynomial function on local time with coefficients previously fitted on few significant terms of Fourier series on time with data from 1998.4 to 2009.4. Therefore, it is still simple-to-use for GNSS users, compared in particular with other suitable approaches such as those based on the Chapman layer assumption (Hoque and Jakowski 2013) or on electron density fields from climatic models like IRI (Zus et al. 2016), because only one additional parameter μ_2 ,which is the shape function of the topside layer, is required.

Two Layer Assumption

When GIMs, or any VTEC model, are used to correct the ionospheric delay in space geodetic measurements like GNSS, the slant delay for each signal is computed by multiplying the vertical delay at the IPP location by an obliquity factor, i.e., a mapping function under the single layer assumption. The most commonly used mapping function, which will be called the standard mapping function in this study, is described:

where STEC is computed along the signal ray-path and VTEC, and are defined at IPP (Figure 1).

We take advantage of the two-layer tomographic approximation implemented in the TOMION (TOmographic Model of the IONosphere) software (Hernández-Pajares et al. 1997) for the daily computation of UPC GIMs since the IGS Ionospheric Working Group started, on June 1, 1998 (Hernández-Pajares et al. 2009). Indeed, the ionospheric electron content by two spherical geocentric layers is significantly better for fitting the ground-based GNSS measurements than the single-layer and for computing the VTEC (Hernández-Pajares et al. 1997, 1999, Juan et al. 1997). The first ionosphere layer is defined between 110 km and 790 km with a central height of 450 km, as the assumed effective height in VTEC GIMs generated within IGS, and the second layer is from 790 km to 1470 km, coinciding with the topside electron content for GPS missions on board Low Earth Orbiting satellites like FORMOSAT-3/COSMIC, with a central height of 1130 km (Figure 2). Although the thickness of the condensed ionosphere is 1360 km (1470 km-110 km), actually it includes the whole ionosphere and plasmasphere up to GPS height with the two respective effective heights, which are the central values of 450 km and 1130 km. The corresponding geometric factors, denoted by M_1 and M_2, are used in the UPC TOMION runs to estimate the vertical distribution of electron content among the top and bottom voxels.

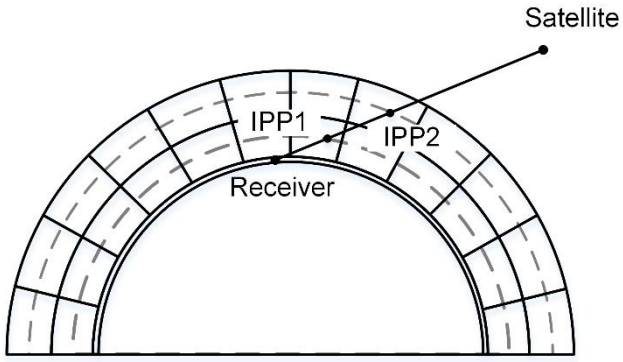

Fig. 2 Segmentation diagram of STEC for a given GNSS ray under the two-layer assumption. IPP1 and IPP2 are the intersection points of the receiver-to-satellite line of sight with the first and the second central heights, respectively.

136 We define two ratio values μ_1 and μ_2 as follows:

$$\mu_1 = \frac{N_1}{V} = \frac{P_1}{V}$$

$$\mu_2 = \frac{N_2}{V} = \frac{P_2}{V}$$

137 where N_1 and N_2 are the mean electron densities for the first and second layers, respectively.
138 V is VTEC for the whole ionosphere, and P_1 and P_2 are the partial vertical electron contents
139 for the first and second layer, respectively. Assume that the vertical profile is simplified as
140 just two points, instead of hundreds of points when it is estimated from radio occultation
141 measurements inversion (Hernández-Pajares et al. 2000b). Here, the ratios μ_1 and μ_2 can be
142 interpreted as a coarse shape function of only the bottomside and topside layers respectively,
143 i.e. the relative ratio of mean electron density N_1 and N_2 respectively. So these ratios are also
144 equivalent to vertical partial electron contents for the first and second layers, as both layers
145 have equal thicknesses.

146 In order to simplify applying μ_2 and μ_1, obtained from the database of UPC TOMION,
147 for any VTEC model user the given slant TEC can be divided into two parts by neglecting the
148 horizontal gradients within each layer:

$$STEC = \frac{H}{\cos z'} \cdot N_1 + \frac{H}{\cos z''} \cdot N_2$$

149 where H is the thickness of each layer; are the length of the part of the ray included
150 in the first layer and in the second layer; and are the electron density of the first layer
151 and the second layer where the ray passes; , are the partial vertical electron contents of
152 each layer crossed by the GNSS ray (partial electron content); , are VTECs for the whole
153 ionosphere at IPP1 and IPP2, respectively; , are the second-layer shape function of the
154 volume element (voxel) corresponding to IPP1 and of the voxel of IPP2; , are the
155 standard mapping functions at IPP1 and IPP2 equals to and respectively.

156 Since μ_2 refers to the shape function of the second layer, this ratio "summarizes" the
157 vertical distribution of ionospheric electron density. Equation (3) presents the idea of the

Barcelona Ionospheric Mapping function (BIMF). In order to apply the new mapping function we can consider two approaches:

1) μ_2 could be directly based on the daily UPC tomographic runs, after grid interpolation and applied in a similar way as the GIMs (IONEX format).

2) Another approach, more challenging from the point of view of mapping function determination but simpler for a user application, is to model μ_2 as a function of space and time for a given range of latitudes, such as mid-latitudes. In this way the user does not need any external information, contrary to the previous approach. In the next part, μ_2 variation characteristics will be analyzed in this regard.

μ_2 daily variation characteristics

TOMION was developed at UPC by the second author to compute the daily GIMs in the context of IGS. Its application on a daily basis started on June 1, 1998, using a 2-layer tomographic approach that takes into consideration the distribution of the electrons in the outer part of the ionosphere. The resulting Global Ionospheric Maps, using Kriging interpolation and provided every 15 minutes to the IGS, are identified as "UQRG" (Orús et al. 2005, Hernández-Pajares et al. 2016). Therefore, TOMION runs have provided a valuable long-term database for μ_2 since the mid-1998.

As it can be seen from the example shown in Figure 3, most of the latitude bands show similar daily μ_2 variations, except the southern area of 60°S which is due to the scarcity of data. It can be observed that the upper shape function μ_2 reaches its peak at about 4:00 LT, which is consistent with the expectedly relevant role played by the plasmasphere during the night, and the valley region occurs approximately between 8:00 LT and 17:00 LT. It is noticeable that the μ_2 values are higher at nighttime than those at daytime, which corresponds to the daily variation of vertical electron density distribution. Thus, in order to overcome the limitation brought by the fixed single-layer height, it is reasonable to use μ_2 ratio to improve the standard mapping function.

It is worth mentioning that μ_2 can sometimes assume values outside the interval of [0, 1] when for instance the most part of electron content is above the mean height of the second layer (greater than 1), or below the mean height of the first layer (negative value). Considering that μ_2 is obtained from actual measurements, the mapping VTEC to STEC

189 using μ_2 values is expected to give more realistic results as compared to the standard mapping
190 function approach.

191

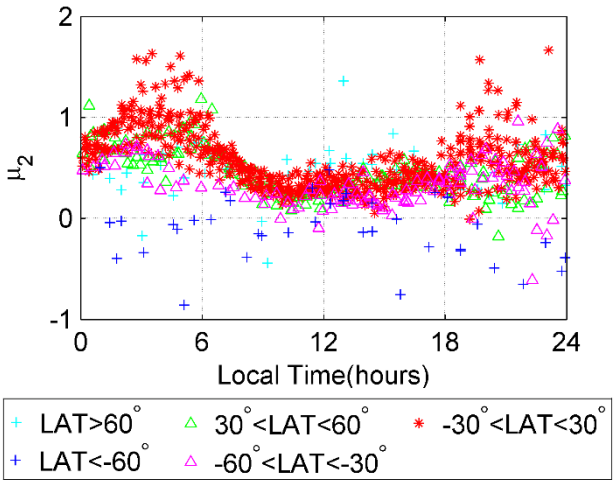

192

193 **Fig. 3** μ_2 daily variations of different latitude ranges on DOY 349, 2006.

194

195 The modelling and assessment of BIMF will be performed during next sections,
196 following the methodology summarized in Figure 4.

197

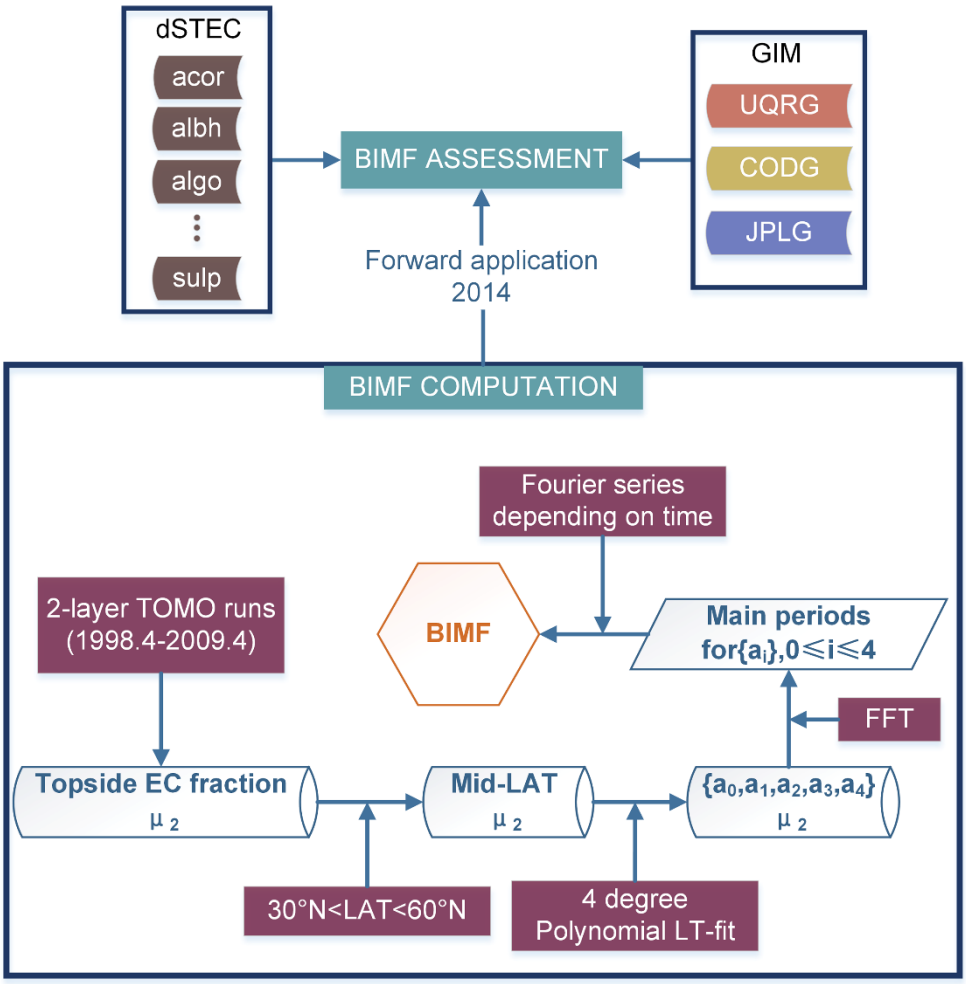

Fig. 4 Diagram of BIMF modeling and assessment.

BIMF modeling based on μ_2

We are focusing on northern mid-latitudes, e.g. Europe, specifically in the latitude range from 30°N to 60°N, as the main research region. For this purpose, the μ_2 variation with respect to latitude is neglected for the area under consideration.

First, for each given day in the study region, the μ_2 parameter is modeled as a 4th-order polynomial of local time, since we realized that such fitting describes the daily μ_2 variation with local time with good compromise between accuracy and simplicity,

(4)

where represents the polynomial coefficients and is the local time for the related day. To solve this linear equation, we use equally-weighted least squares by removing the observation data with residual greater than 3 times the Root Mean Square Error (outliers). The time series

212 of polynomial coefficients (a_0, a_1, a_2, a_3 and a_4) are obtained from the dual-layer TOMION
213 runs during one solar cycle, beginning at year 1998.4. An example for the polynomial fitting
214 for the day 349 of the year 2006 and related daily μ_2 data are given in Figure 5.

215

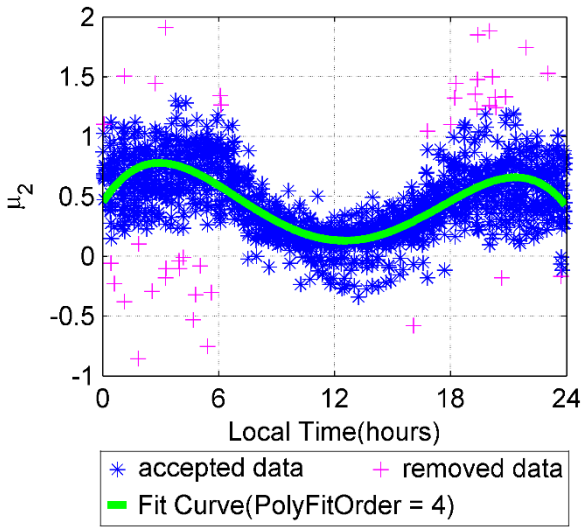

216

217 **Fig. 5** Example of daily variation of polynomial fitting of μ_2 for northern mid-latitudes (DOY
218 349, 2006).

219

220 As a second step, the predominant period terms of each coefficient are determined
221 using a Fast Fourier Transform (FFT) for the 11-year time series, corresponding to one solar
222 cycle period (Table A1 to Table A5). As shown in Figure 6, the coefficients a_1 to a_4 show the
223 clear presence of three main periods corresponding to 365.2, 182.6 and 121.7 days, in
224 concordance with three main seasonal components found for the global electron content
225 variability (Hernández-Pajares et al. 2009). The predominant periods of the constant term a_0
226 are more complex.

227

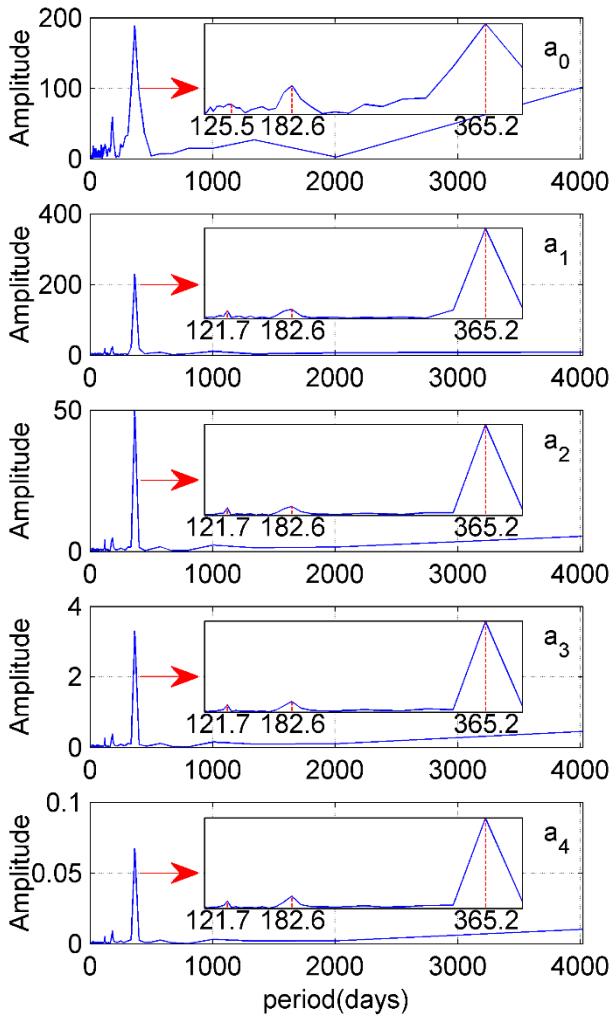

Fig. 6 Fast Fourier transform of five coefficients time series data from the daily TOMION runs from 1998.4 to 2009.4

After analyzing the temporal variation of μ_2, we obtain the μ_2 model. For IPPs with latitudes between 30°N and 60°N, the μ_2 parameter is expressed as a function of the number of days since the modified Julian day 50965 (DOY 152, 1998) and the local time in hours. The 4-order polynomial function o becomes,

(5)

— — (6)

where is local time of IPP and , with mjd is modified Julian day. Further we have: is a constant term; is the coefficients of sine terms; is the coefficients of cosine terms; is the kth period of the polynomial coefficient ; is the

number of dominant periods of .Table A1 to A5 in Appendix A give the values of related parameters.

For each polynomial coefficient, the Fourier series fitting is compared with the data from the first step. As it can be seen from Figure 7, the Fourier series can predict the coefficients for the period not used in the modeling in general well. In the case of the constant term, a_0, there is still room for future modeling, maybe in the context of latitudinal dependence. But, in general, it seems that BIMF is performing reasonably well as a climatological model and might be suitable for prediction of mapping function after direct assessment of the improvement in the STEC retrieval from VTEC models. See the next section.

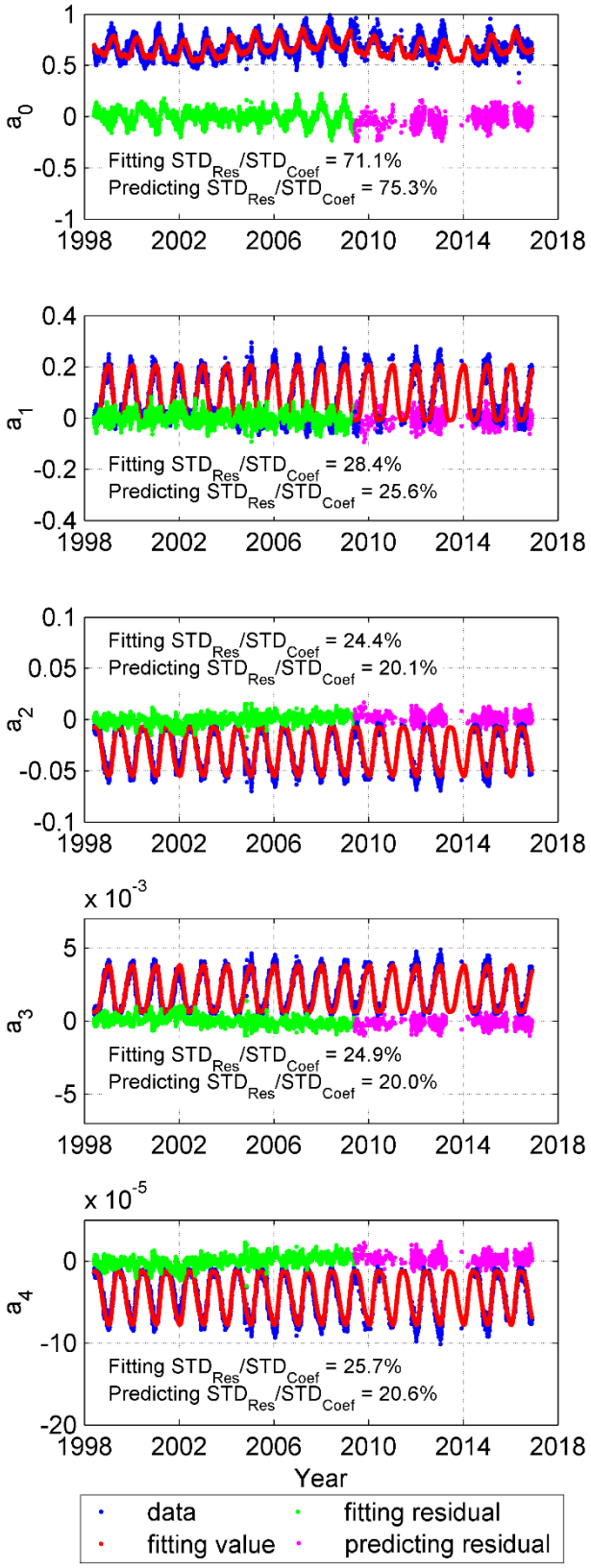

252

253 **Fig. 7** Results of Fourier series fitting of five polynomial coefficients from a_0 to a_4. The in
254 green and pink dots are the residuals for the data used in the regression and the residuals by

using the predicted values, respectively. The percentages of standard deviation (STD) of residuals regarding to the coefficient STD are also given in the plots.

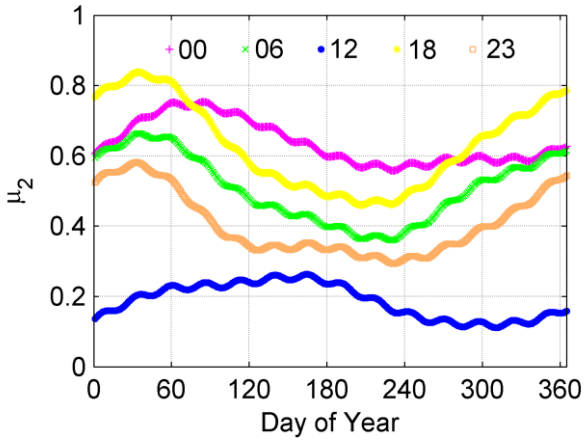

Fig. 8 Predicted values of μ_2 by BIMF-nml during 2014 for different local time vs. day of year.

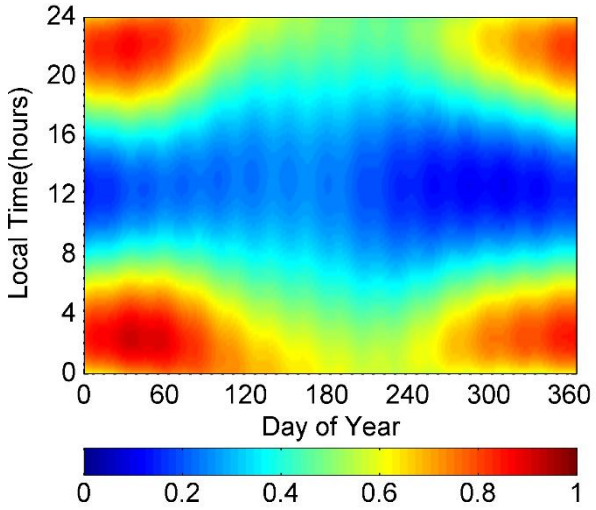

Fig. 9 Predicted values of μ_2 by BIMF-nml during 2014 as a function of local time and day of year.

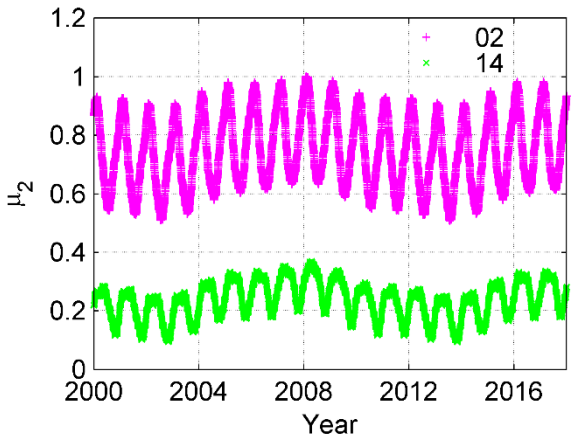

266

267 **Fig. 10** Predicted values of μ_2 by BIMF-nml from 2000 to end of 2017 for the night- and day-
268 time (02h and 14h Local Time).

269

270 The main dependences of the final fitted μ_2 are shown in Figures 8, 9 and 10. In
271 particular in Figure 8, during the whole year 2014, the higher values of μ_2 occur during the
272 nighttime, as expected. Semiannual and almost monthly periods, close to the solar rotation
273 one, can be seen as well, which is in agreement with one previous study (Hernandez-Pajares
274 et al. 2009). A simultaneous view of LT and season dependence is shown in Figure 9, where
275 μ_2 presents the highest values in fall and winter seasons. The dependence along more than
276 one solar cycle is presented in Figure 10, with highest values of μ_2 occurring during solar
277 minimum, indicating a small reduction of the topside electron content compared with the
278 ionosphere reduction (below altimeter). This result is in agreement with the evolution of the
279 bias between altimeter and GNSS VTEC, a proxy of the evolution of the topside electron
280 content reversed in sign, and the evolution of the VTEC below the altimeter. Indeed, as it ca
281 be seen in Figures 1 and 2 of Roma-Dollase et al. (2017) the variation of the ionospheric
282 VTEC is much higher than the variation of the topside VTEC producing there relative
283 minima of mu2 in Solar Maximum (e.g. around 2000-2002, or 2013-2014) and relative
284 maximum in Solar Minimum.

285 Finally, the Barcelona Ionospheric Mapping Function for northern mid-latitudes can
286 be depicted with a revised notation as follows:

287 (7)

288 where and are VTECs at IPP1 and IPP2, respectively; , are standard
289 mapping functions at IPP1 and IPP2, respectively; , are μ_2 ratio values at IPP1
290 and IPP2, respectively.

291

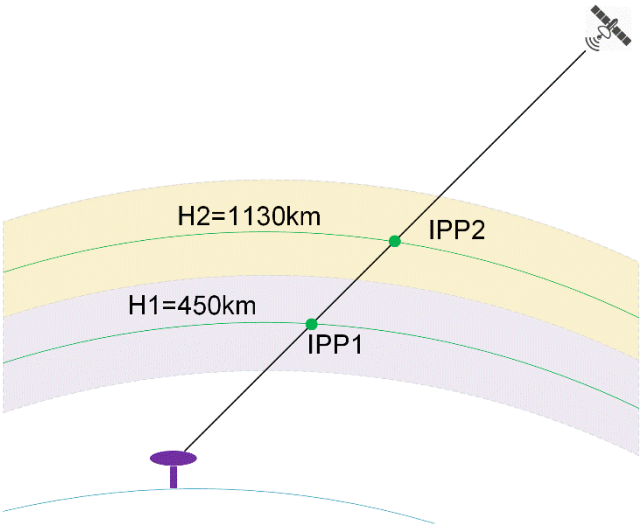

Fig. 11 Diagram showing two ionospheric pierce points involved in BIMF definition.

Assessment

According to previous research (Hernández-Pajares et al. 2017) we can consider for each given receiver-satellite pair, the difference between the GPS geometry-free linear combination of carrier phase at one epoch, in length units, $L_I(t) = L_1(t) - L_2(t)$ and the value at the reference epoch $L_I(t_{ref})$ corresponding to the highest elevation in the phase-continuous arc of data. This value, $= L_I(t) - L_I(t_{ref})$, provides a very precise ionospheric truth of the STEC referred to the value at maximum elevation, dSTEC (ΔS), in space and time.

Indeed, we can write $\Delta S = \alpha \, \Delta L_I$, with being $\alpha = f_1^2 f_2^2 / 40.3(f_1^2 - f_2^2) \simeq (10/1.05)$ TECU/m $\simeq$ 9.52 TECU/m. Such a ΔS value is very accurate, reflecting the level of the carrier phase measurement noise and multipath, i.e., it is typically much below 0.1 TECU and becomes an excellent reference for VTEC (V, in TECU) provided by GIMs, and for any mapping function, M. Indeed the corresponding ΔS error, ε, can be obtained in a straightforward way as $\varepsilon \simeq \alpha \, \Delta L_I - \Delta(M \bullet V)$.

The STEC value at one epoch minus the STEC at maximum elevation, dSTEC, is typically provided every 30 seconds with an accuracy of better than 0.1 TECU. But the pairs of observations that are very close in elevation, i.e. less than 20º, should be removed because they are associated with very small STEC differences, insensitive to the accuracy of the model. Some of the previous usages of dSTEC test can be seen in Orús et al. (2005) and Feltens et al. (2011), and more recently Hernández-Pajares et al. (2017). This test has been used to compare the performances of different ionospheric models in the IGS context (Hernández-Pajares et al. 2016). In addition, the dSTEC observable is very sensitive to the

316 changes in the elevation. All in all, it can be considered as a good ionospheric reference truth
317 for the assessment of any ionospheric mapping function when a minimum elevation
318 difference, e.g. 20º as indicated above, regarding the highest-elevation reference value per
319 arc, is taken.

320 In order to evaluate the performance of BIMF, we have considered:

321 1) The dSTEC data for the whole year 2014 from all the available IGS stations,
322 which are not used for the generation of the UQRG GIMs in the studied region,
323 has been selected to ensure external electron content information, following the
324 recommendations given in Hernández-Pajares et al. 2017. Here, the latitude range
325 of the selected stations is narrowed to 35°N to 55°N to assure the latitude of IPPs
326 is in the modeling region (30°N to 60°N). There are 14 stations available in the
327 specific range, but only 8 of them, marked in black in Figure 12, have enough data
328 for statistics.

329 2) Several statistical parameters to perform the comparisons. Namely:

330 a) The daily RMS(Root Mean Square) of the dSTEC error experienced by each
331 GIM (hereinafter DRMSE) with BIMF versus the corresponding error using
332 the classical mapping functions at 450 km (IGS) and 350 km (SBAS)
333 effective heights.

334 b) Percentage of days for which BIMF is performing better, i.e. with lower
335 dSTEC RMS error (DRMSE), than the classical mapping functions
336 (hereinafter PDBB). This is done regarding the number of days, expressed in
337 "Sample Number" in Table 1, B1 and B2, for which each given receiver was
338 selected. As mentioned before, to guarantee a fair assessment, the receivers
339 are selected when they have not been used in the GIMs computation.

340 c) Percentage of DRMSE referred to the daily RMS of the observed dSTEC
341 values (DRMS), hereinafter PDE[%] = 100*DRMSE/DRMS.

342 d) Relative reduction of PDE for BIMF compared with PDE for the classical
343 mapping functions, hereinafter RPDE[%] = PDE[classic]-PDE[BIMF].

344

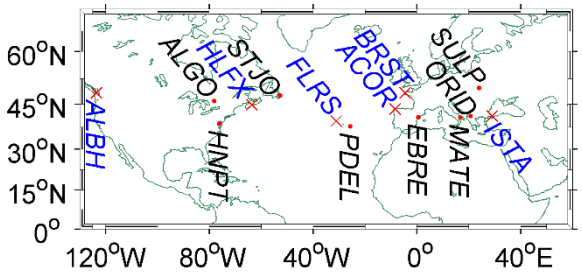

Fig. 12 IGS stations that are not used for the generation of UQRG GIM in 2014 and are used for external assessment of the BIMF performance. The stations in blue were not used for statistical purposes due to very limited data in only a few available days in which the stations are not used for GIM computation.

Considering different single-layer heights for different applications, typically 450 km for GIM and 350 km for SBAS, standard mapping functions with the single-layer height of both 450 km and 350 km are compared with BIMF. For simplification, we use S450 and S350 to represent standard mapping functions with shell height 450 km and 350 km respectively in this context.

By taking the station ORID as an example, it is obvious that daily RMS of dSTEC residual error DRMSE with BIMF is smaller than that with the standard mapping function, particularly for the signals gathered at low elevation (Figure 13). Specifically, from DOY 16 to 30, the DRMSE has been reduced by approximately 0.5 to nearly 1.0 TECU. The results of the 234-day analysis in 2014, shown in Figure 14, indicates that BIMF performs better than standard mapping function in 210 days in terms of RMSE, i.e. PDBB more than 90%.

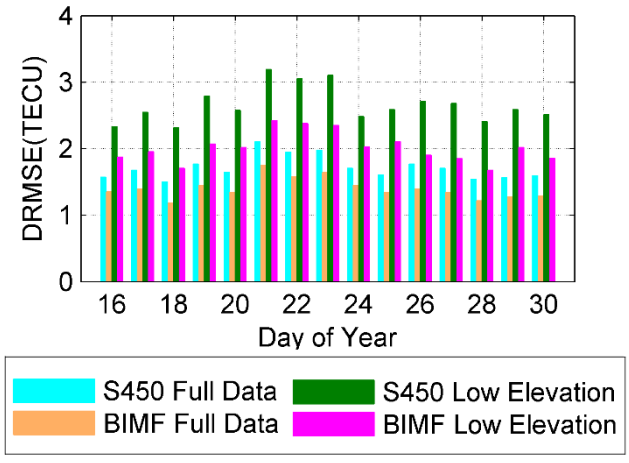

Fig. 13 ORID station: dSTEC daily RMSE with BIMF and S450 for UQRG GIMs from DOY 16 to 30, 2014. The bars in cyan and in orange are the results for all data. The bars in

365 green and in pink are the results for the elevation of the given line-of-sight ray lower than
366 40°, and the difference with the reference ray of at least 20° above.

367

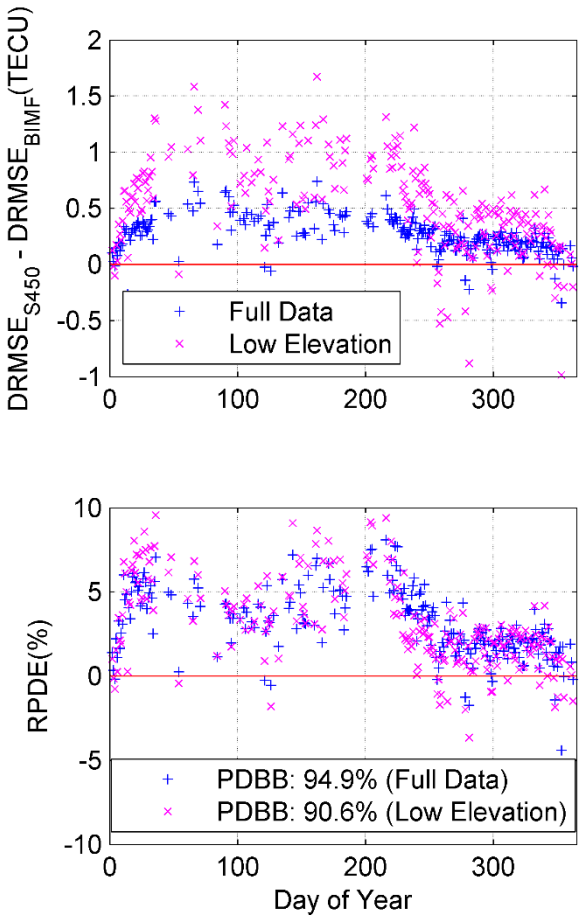

368

369 **Fig. 14** ORID station: the differences of dSTEC daily RMSE with S450 minus dSTEC daily
370 RMSE with BIMF for 234 days during the year 2014, applied on the UQRG GIMs. The
371 upper plot is absolute differences and the bottom plot is the percentage of differences with
372 respect to the dSTEC daily RMS.

373

374 As for the 8 IGS stations identified for computing statistics, BIMF applied to UQRG
375 GIM performs well for six stations, but not for stations *ALGO* and *STJO*, which present high
376 geomagnetic latitudes stations (Table 1). The BIMF performance might be improved in the
377 future when a global BIMF model based on solar-magnetic local time and latitude can be
378 developed. The number of days where the dSTEC RMSE (DRMSE) are decreased accounts
379 for more than 70% of available days in 2014. Meanwhile, CODG GIM and JPLG GIM are
380 also used for assessment (Table 2), showing still larger reductions of dSTEC error, with

RPDE up to 22% and 20% for 2014 respectively, compared to the results of BIMF applied on UQRG GIM with up to 8% of improvement, which GIM was already estimated with the dual-layer tomographic model. As shown in the Table B2, the BIMF improved dSTEC using JPLG GIM as well dominantly, with an improvement given by PDDB in more than 70% of the cases. From all the 14 available stations, ten stations have a PDDB over 90% for low-elevation statistics. This reinforces the physical consistency of BIMF, regardless of the UPC-TOMION model used originally to compute it.

Table 1 Statistics Results of different stations using UQRG in 2014, focusing on the percentage when the daily $RMSE_{BIMF}$ is lower than the daily $RMSE_{S450}$ (PDBB).

Site Name	Geographic Latitude	Geographic Longitude	Geomagnetic Latitude	PDBB		Sample Number
				Full Data	Low Elevation	
ALGO	45.96°N	78.07°W	55.46°N	39.2%	32.7%	171
EBRE	40.82°N	0.49°E	42.79°N	72.9%	69.1%	188
HNPT	38.59°N	76.13°W	48.13°N	72.8%	71.5%	239
MATE	40.65°N	16.70°E	39.89°N	93.7%	86.1%	252
ORID	41.13°N	20.79°E	39.67°N	94.9%	90.6%	234
PDEL	37.75°N	25.66°W	43.84°N	86.7%	88.0%	241
STJO	47.60°N	52.68°W	56.44°N	24.3%	42.8%	173
SULP	49.84°N	24.01°E	47.61°N	78.3%	74.8%	115

Table 2 BIMF compared to Standard Mapping Function with the fixed height 450 km and 350 km for different GIM products in 2014: Percentage of days with reduced daily RMSE (PDBB) and Percentage of daily RMSE maximum reduction (maximum RPDE) for all stations. For UQRG GIM, stations *ALGO* and *STJO* are excluded.

GIM	PDBB range				Range of maximum RPDE			
	Full Data		Low Elevation		Full Data		Low Elevation	
	450 km	350 km	450 km	350 km	450 km	350 km	450 km	350 km

UQRG*	[72.8%, 94.9%]	[90.4%, 98.8%]	[69.1%, 90.6%]	[87.8%, 98.7%]	[4.4%, 8.1%]	[8.8%, 14.7%]	[5.9%, 10.6%]	[11.6%, 18.4%]
CODG	[48.3%, 84.1%]	[71.8%, 95.9%]	[48.5%, 80.4%]	[70.8%, 95.9%]	[4.1%, 22.1%]	[7.9%, 32.0%]	[5.5%, 13.7%]	[8.9%, 22.7%]
JPLG	[78.7%, 98.4%]	[90.6%, 100 %]	[71.3%, 99.2%]	[88.1%, 100%]	[5.0%, 20.8%]	[9.3%, 28.7%]	[5.9%, 18.0%]	[11.6%, 25.9%]

Conclusions

Focusing on the GNSS users in the latitude region of about 30°N and 60°N, such as Europe, a new mapping function BIMF is climatologically defined. The BIMF is based on the database of dual-layer tomographic daily calculations performed at UPC as one of the IGS ionospheric analysis centers since 1998. The new mapping function is proposed for GNSS users to improve the accuracy of conversion from VTEC to STEC. The key parameter of BIMF is μ_2, that is, the shape function value at the second layer. As a first step, we analyzed the variation of the second layer shape function μ_2 for northern mid-latitudes. As noted, only local-time daily variation has been taken into account in this work. It is found that there exist obvious variation features during one day and one solar cycle. Then according to these findings, the μ_2 model is established, which is of climatic-type and can be used for predictions. BIMF is simple to apply for STEC computation by saving the coefficients of the μ_2 model as constants.

In terms of model assessment, the GIMs from different IGS Ionosphere Associate Analysis Centers are used to obtain the VTEC values, and precise dSTEC measurements are chosen as evaluation criteria. Only the IGS stations not used for the generation of GIMs are selected to test the performance of BIMF. From the statistical results of daily RMSE in 2014, it is shown that BIMF performs better than standard mapping function in the most cases for all mid geomagnetic latitudes, and with VTEC GIMs computed with different models by different analysis centers, not only UPC but especially others like CODE and JPL. The new mapping function will be optimized and generalized for different latitudinal ranges in the future. At the moment the current results prove the potential prospects of BIMF for northern mid-latitudes. As future work we plan to generalize BIMF at a global scale, extending as well the type of validation to the positioning domain.

Acknowledgements

This research has been generated within the AUDITOR project (Advanced Multi-Constellation EGNSS Augmentation and Monitoring Network and its Application in Precision Agriculture), funded by the European Union's H2020 Programme, under grant agreement number 687367. The first author is grateful to the financial support of the China Scholarship Council. The authors are grateful as well with the International GNSS Service. The open-data open-product scientific organizations always provide a professional and friendly framework for collaboration. The authors would like to thank the Editor Alfred Leick and the anonymous reviewers for their valuable comments and suggestions to improve the quality of the paper. The second author is indebted to Dr. Raül Orús-Pérez for his suggestions to improve the last version of the manuscript.

Appendix A

Table A1 Coefficients of a_0

0			6.778886E-01
1	365.2	-8.688163E-02	3.578382E-02
2	4017.0	-4.430154E-02	2.439461E-02
3	182.6	-1.869270E-02	-2.323595E-02
4	1339.0	-1.333096E-02	-1.128014E-03
5	125.5	-1.006658E-02	-3.188399E-03
6	26.43	-6.209667E-03	-6.513369E-03

Table A2 Coefficients of a_1

0			8.854738E-02
1	365.2	-4.889833E-02	-1.037872E-01
2	182.6	1.211679E-02	5.830693E-04
3	121.7	8.548938E-03	5.303727E-03

Table A3 Coefficients of a_2

0			-2.925523E-02
1	365.2	1.111281E-02	2.224605E-02

2	182.6	-2.409684E-03	4.900974E-04
3	121.7	-1.681305E-03	-1.170320E-03

Table A4 Coefficients of a_3

0			2.062601E-03
1	365.2	-7.358248E-04	-1.475076E-03
2	182.6	1.864769E-04	-4.539838E-05
3	121.7	1.047826E-04	8.154671E-05

Table A5 Coefficients of a_4

0			-4.167004E-05
1	365.2	1.478527E-05	3.013404E-05
2	182.6	-4.442136E-06	1.020289E-06
3	121.7	-2.044199E-06	-1.758158E-06

Appendix B

Table B1 Statistical results for different stations using CODG in 2014

Site Name	Geomagnetic Latitude	PDBB		Sample Number
		Full Data	Low Elevation	
ACOR	46.73°N	56.4%	48.5%	202
ISTA	38.30°N	84.1%	80.4%	244
ORID	39.67°N	66.5%	63.1%	236
SULP	47.61°N	48.3%	50.0%	118

Table B2 Statistical results for different stations using JPLG in 2014

Site Name	PDBB		Sample Number
	Full Data	Low Elevation	

ACOR	78.7%	71.3%	202
ALBH	98.4%	99.2%	248
ALGO	89.6%	91.2%	251
EBRE	79.5%	87.0%	239
FLRS	89.1%	94.8%	248
HLFX	90.1%	94.4%	252
HNPT	96.3%	98.3%	240
ISTA	98.4%	98.4%	245
MATE	91.7%	96.8%	252
ORID	96.2%	97.0%	236
PDEL	81.0%	95.2%	248
STJO	84.0%	88.0%	250
SULP	96.6%	95.8%	118

449

450 **References**

451 Birch MJ, Hargreaves JK, Bailey GJ (2002) On the use of an effective ionospheric height in
452 electron content measurement by GPS reception. Radio Science, 37(1),
453 doi:10.1029/2000RS002601

454 Dow JM, Neilan RE, Rizos C (2009) The international GNSS service in a changing landscape
455 of global navigation satellite systems. Journal of Geodesy, 83(3):191-198

456 European Commission (2016) European GNSS (Galileo) Open Service Ionospheric
457 Correction Algorithm for Galileo Single Frequency Users, Issue 1.2

458 Feltens J, Angling M, Jackson-Booth N, Jakowski N, Hoque M, Hernández-Pajares M,
459 Aragón-Àngel A, Orús R and Zandbergen R (2011) Comparative testing of four
460 ionospheric models driven with GPS measurements. Radio Science, 46(6):RS0D12

461 Hernández-Pajares M, Juan JM, Sanz J (1997) Neural network modeling of the ionospheric
462 electron content at global scale using GPS data. Radio Science, 32(3):1081-1089

463 Hernández-Pajares M, Juan JM, Sanz J (1999) New approaches in global ionospheric
464 determination using ground GPS data. Journal of Atmospheric and Solar-Terrestrial
465 Physics, 61(16):1237-1247

Hernández-Pajares M, Juan JM, Sanz J, Colombo OL (2000a) Application of ionospheric tomography to real-time GPS carrier-phase ambiguities resolution, at scales of 400-1000 km and with high geomagnetic activity. Geophysical Research Letters, 27(13):2009-2012

Hernández-Pajares M, Juan JM, Sanz J (2000b) Improving the Abel inversion by adding ground GPS data to LEO radio occultations in ionospheric sounding. Geophysical Research Letters, 27(16):2473-2476

Hernández-Pajares M, Juan JM, Sanz J, Colombo OL (2002) Improving the real-time ionospheric determination from GPS sites at very long distances over the equator. Journal of Geophysical Research: Space Physics, 107(A10):SIA 10-1-SIA 10-10

Hernández-Pajares M, Juan JM, Sanz J, Orus R, García-Rigo A, Feltens J, Komjathy A, Schaer SC, Krankowski, A (2009) The IGS VTEC maps: a reliable source of ionospheric information since 1998. Journal of Geodesy, 83(3):263-275

Hernández-Pajares M, Roma-Dollase D, Krankowski A et al. (2016) Comparing performances of seven different global VTEC ionospheric models in the IGS context. International GNSS Service Workshop (IGS 2016): Sydney, Australia, February 8-12

Hernández-Pajares M, Roma-Dollase D, Krankowski A, García-Rigo, A, Orús-Pérez R (2017) Methodology and consistency of slant and vertical assessments for ionospheric electron content models. Journal of Geodesy, 91(12):1405-1414

Hoque MM, Jakowski N (2013) Mitigation of ionospheric mapping function error. Proc. ION GNSS+ 2013, Nashville Convention Center, Nashville, Tennessee, USA, September 16-20, 1848-1855

Juan JM, Rius A, Hernández-Pajares M, Sanz J (1997) A two-layer model of the ionosphere using Global Positioning System data. Geophysical Research Letters, 24(4):393-396

Klobuchar JA (1987) Ionospheric time-delay algorithm for single-frequency GPS users. IEEE Transactions on Aerospace and Electronic Systems, 23(3):325-331

Komjathy A, Langley RB (1996) The effect of shell height on high precision ionospheric modelling using GPS. Proceedings of the 1996 IGS Workshop, Silver Spring, Maryland, USA, March 19-21, 193-203

Komjathy A, Sparks L, Mannucci AJ, Coster A (2004) The ionospheric impact of the October 2003 storm event on WAAS. Proc. ION GNSS 2004, Long Beach Convention Center, Long Beach, California, USA, September 21-24, 1298-1307

Niranjan K, Srivani B, Gopikrishna S, Rama Rao PVS (2007) Spatial distribution of ionization in the equatorial and low-latitude ionosphere of the Indian sector and its effect on the pierce point altitude for GPS applications during low solar activity periods. Journal of Geophysical Research: Space Physics, 112(A5):A05304

Lejeune R, El-Arini MB, Doherty P, Klobuchar J, De Paula E, Rodrigues F, Canavitsas A (2001) Performance of SBAS ionospheric estimation in the equatorial region. Proc. ION GPS/GNSS 2003, Oregon Convention Center, Portland, Oregon, USA, September 9-12, 1658-1669

Roma-Dollase D, Hernández-Pajares M, Krankowski A, et al (2017) Consistency of seven different GNSS global ionospheric mapping techniques during one solar cycle. Journal of Geodesy. https://doi.org/10.1007/s00190-017-1088-9

Sakai T, Yoshihara T, Saito S, Matsunaga K, Hoshinoo K, Walter T (2009) Modeling Vertical Structure of Ionosphere for SBAS. Proc. ION GNSS 2009, Savannah International Convention Center, Savannah, Georgia, USA, September 22-25, 1257-1267

Orús R, Hernández-Pajares M, Juan JM, Sanz J (2005) Improvement of global ionospheric VTEC maps by using kriging interpolation technique. Journal of Atmospheric and Solar-Terrestrial Physics, 67(16):1598-1609

Schaer S. (1999) Mapping and predicting the Earth's ionosphere using the Global Positioning System. Ph.D. Thesis, Astronomical Institute, University of Berne, Switzerland

Zus F, Deng Z, Heise S, Wickert J (2016) Ionospheric mapping functions based on electron density fields. GPS Solutions, 21(3):873-885

Author Biographies

Haixia Lyu received her Bachelor degree in 2010, and Master degree in 2012, both from Wuhan University, and she is a Ph.D. candidate at GNSS Research Center, Wuhan University and now is visiting UPC-IonSAT from 2016 where the focus of her current research lies in ionospheric determination using GNSS data.

Manuel Hernández-Pajares is presently a Full Professor at UPC, Barcelona. He is working on GPS since 1989 (at ICC at such a time). Since 1994 he has focused on new algorithms for precise ionospheric sounding and GNSS navigation. He has been the chair of the

International GNSS Service (IGS) Ionosphere WG (2002-2007), among other projects and responsibilities. He created the new research group, UPC-IonSAT, in Nov. 2013.

Metin Nohutcu received his Ph.D. degree from Middle East Technical University (METU) in 2009. Currently, he is an assistant professor at Hacettepe University, Geomatics Engineering Department. His research interests include ionosphere modeling with GNSS data, determination of ionospheric effective height and precise GNSS positioning.

Alberto García-Rigo is an international expert on GNSS ionospheric determination, space weather, and positioning, with a particular focus on real-time/prediction operational systems. He is working as Research Director at UPC, and he has been a co-founder of UPC-IonSAT research group. He is the chairman of IAG's Real-Time Ionosphere Monitoring Working Group, and he has been actively collaborating in IGS Ionosphere Working Group for the last decade.

Hongping Zhang is a professor at Wuhan University, China. Dr. Zhang received his doctorate degree in GNSS precise data processing and application in 2006. His main research interests include GNSS/ionosphere inversion research and GNSS/INS coupling integration.

Jingnan Liu is a member of Chinese Academy of Engineering. He graduated from Wuhan Institute of Surveying and Mapping (current Wuhan University) and received his Master degree in 1982. He has been engaged in the application research of geodetic theory and has made a series of outstanding contributions in coordinate system theory, application and software development of satellite positioning, especially in the field of GNSS application in engineering.